ELSEVIER

A damage model for the simulation of delamination in advanced composites under variable-mode loading

A. Turon [a], P.P. Camanho [b,*], J. Costa [a], C.G. Dávila [c]

[a] *AMADE, Polytechnic School, University of Girona, Campus Montilivi s/n, 17071 Girona, Spain*
[b] *DEMEGI, Faculdade de Engenharia, Universidade do Porto, Rua Dr. Roberto Frias, 4200-465 Porto, Portugal*
[c] *NASA Langley Research Center, Hampton, Virginia, USA*

Abstract

A thermodynamically consistent damage model is proposed for the simulation of progressive delamination in composite materials under variable-mode ratio. The model is formulated in the context of Damage Mechanics. A novel constitutive equation is developed to model the initiation and propagation of delamination. A delamination initiation criterion is proposed to assure that the formulation can account for changes in the loading mode in a thermodynamically consistent way. The formulation accounts for crack closure effects to avoid interfacial penetration of two adjacent layers after complete decohesion. The model is implemented in a finite element formulation, and the numerical predictions are compared with experimental results obtained in both composite test specimens and structural components.
© 2005 Elsevier Ltd. All rights reserved.

1. Introduction

Structural collapse in a composite structure is caused by the evolution of different types of damage mechanisms, such as matrix transverse cracking, fiber fracture and delamination. The particular damage modes depend upon loading, geometry, lay-up and stacking sequence.

Delamination is one of the most common types of damage in laminated fiber-reinforced composites due to their relatively weak interlaminar strengths.

Delamination may arise under various circumstances, such as in the case of transverse concentrated loads caused by low velocity impacts. This damage mode is particularly important for the structural integrity of composite structures because it is difficult to detect during inspection. Furthermore, delamination causes a drastic reduction of the bending stiffness of a composite structure and, when compressive loads are present, promotes local buckling.

When other material non-linearities can be neglected, methods based on Linear Elastic Fracture Mechanics (LEFM) have been proven to be effective in predicting delamination growth. However, LEFM cannot be applied without an initial

* Corresponding author. Tel.: +351 22 5081753; fax: +351 22 5081584.
E-mail address: pcamanho@fe.up.pt (P.P. Camanho).

crack. In some situations, methods combining a stress analysis with a characteristic distance have been applied to predict the initiation of delamination (Camanho and Matthews, 1999; Dávila and Johnson, 1993). After delamination onset, LEFM can be used to predict delamination growth (Liu, 1999; Zou et al., 2002). Techniques such as virtual crack closure technique (VCCT) (Irwin, 1957; Rybicki and Kanninen, 1977; Raju, 1987; Zou et al., 2001; Krueger, 2002), J-integral method (Rice, 1968), virtual crack extension (Hellen, 1975) and stiffness derivative (Parks, 1974) have often been used to predict delamination growth. These techniques are used to calculate the components of the energy release rate. Delamination growth is predicted when a combination of the components of the energy release rate is equal to, or greater than, a critical value (Griffith, 1921).

However, difficulties are also encountered when these techniques are implemented using finite element codes. The calculation of fracture parameters, e.g. stress intensity factors or energy release rates, requires nodal variable and topological information from the nodes ahead and behind the crack front. Such calculations can be done with some effort for a stationary crack, but can be extremely difficult when progressive crack propagation is involved.

Another approach to the numerical simulation of the delamination can be developed within the framework of Damage Mechanics. Models formulated using Damage Mechanics are based on the concept of the cohesive crack model: a cohesive damage zone or softening plasticity is developed near the crack front. The origin of the cohesive crack model goes back to Dugdale (1960) who introduced the concept that stresses in the material are limited by the yield stress and that a thin plastic zone is generated in front of the notch. Barenblatt (1962) introduced cohesive forces on a molecular scale in order to solve the problem of equilibrium in elastic bodies with cracks. Hillerborg et al. (1976) proposed a model similar to the Barenblatt model, but where the concept of tensile strength was introduced. Hillerborg's model allowed for existing cracks to grow and, even more importantly, also allowed for the initiation of new cracks.

Cohesive damage zone models relate tractions to displacement jumps at an interface where a crack may occur. Damage initiation is related to the interfacial strength, i.e., the maximum traction on the traction–displacement jump relation. When the area under the traction–displacement jump relation is

equal to the fracture toughness, the traction is reduced to zero and new crack surfaces are formed. The advantages of cohesive zone models are their simplicity and the unification of crack initiation and growth within one model. Moreover, cohesive zone formulations can also be easily implemented in finite element codes using decohesion elements (Allix et al., 1995; Allix and Corigliano, 1996; Schellekens and de Borst, 1993; Chaboche et al., 1997; Mi et al., 1998; Chen et al., 1999; Alfano and Crisfield, 2001; Camanho et al., 2003; Goyal-Singhal et al., 2004). Although the cohesive damage models cannot be considered non-local damage models (Bažant and Jirásek, 2002), they allow a mesh-independent representation of material softening, provided that the mesh is sufficiently refined.

In the formulation of the cohesive models, it is important to control the energy dissipation during delamination growth in order to avoid the restoration of the cohesive state, i.e., it is necessary to assure that the model satisfies the Clausius–Duhem inequality. There are some models in the literature that can be used under constant mixed-mode conditions (Mi et al., 1998; Alfano and Crisfield, 2001; Camanho et al., 2003; Yan et al., 2001; Li and Wisnom, 1994; Petrossian and Wisnom, 1998; Tvergaard and Hutchinson, 1993; Ladevèze et al., 1998; Borg et al., 2002; Jansson and Larsson, 2001). However, the models proposed generally do not satisfy the Clausius–Duhem inequality under variable-mode loading situation. Most of the models cited above define the damage threshold parameter as the maximum displacement. This assumption may lead to the violation of the Clausius–Duhem inequality when the crack grows in a varying mode.

The restoration of the cohesive state is illustrated in Fig. 1. This figure represents the traction (τ)- relative displacement (Δ) relation for two different mode ratios, $G_{\mathrm{II}}/(G_{\mathrm{II}} + G_{\mathrm{I}}) = A$ (Fig. 1(a)) and $G_{\mathrm{II}}/(G_{\mathrm{II}} + G_{\mathrm{I}}) = B$ (Fig. 1(b)), where G_{I} and G_{II} are the components of the energy release rate. If the mode ratio changes from A to B during delamination growth, there is a restoration of the cohesive state. This effect is clearly inconsistent with the thermodynamical principles.

A damage model for the simulation of delamination under variable-mode is presented in this paper. A new delamination initiation criterion is proposed. The delamination onset criterion stems from the expression of the critical energy release rate for delamination propagation under mixed-mode loading proposed by Benzeggagh and Kenane (1996).
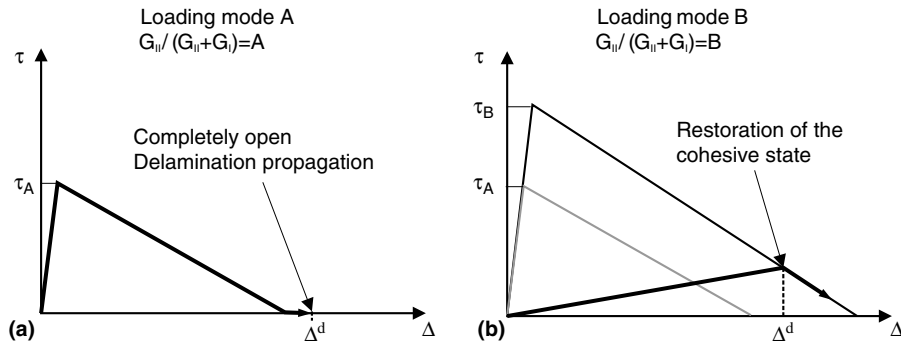
Fig. 1. Restoration of the cohesive state for delamination propagation under variable-mode ratio.

The model is implemented in the implicit finite element code ABAQUS (Anon., 1996) by means of a user-written decohesion element.

This paper is structured as follows: first, the formulation of the damage model for the simulation of delamination onset and growth model is presented. The finite element discretization of the boundary value is described. Finally, the numerical predictions are compared with experimental results obtained in composite test specimens and composite structural components.

2. Model for delamination onset and propagation

The boundary value problem, the kinematic equations, and the constitutive relations are presented for the formulation of the model for delamination onset and delamination propagation.

2.1. Boundary value problem

Consider a domain Ω, as shown in Fig. 2(a), containing a crack Γ_c. The part of the crack on which a cohesive law is active is denoted by Γ_{coh} and is called the fracture process zone (FPZ).

Prescribed tractions, t_i, are imposed on the boundary Γ_F, whereas prescribed displacements are imposed on Γ_u. The stress field inside the domain, σ_{ij}, is related to the external loading and the closing tractions τ_j^+, τ_j^- in the cohesive zone through the equilibrium equations:

$$\sigma_{ij,j} = 0 \quad \text{in } \Omega \tag{1}$$

$$\sigma_{ij}n_j = t_i \quad \text{on } \Gamma_F \tag{2}$$

$$\sigma_{ij}n_j^+ = \tau_i^+ = -\tau_i^- = \sigma_{ij}n_j^- \quad \text{on } \Gamma_{coh} \tag{3}$$

2.2. Kinematics of the interfacial surface

To develop the necessary kinematic relationships, consider the crack Γ_c shown in Fig. 2(a) as part of a material discontinuity, Γ_d, which divides the domain Ω into two parts, Ω_+ and Ω_- (Fig. 2(b)).

The displacement jump across the material discontinuity Γ_d, $[\![u_i]\!]$, can be written as

$$[\![u_i]\!] = u_i^+ - u_i^- \tag{4}$$

where $u_i^\pm$ denotes the displacement of the points on the surface of the material discontinuity Γ_d of the parts $\Omega_\pm$ of the domain.
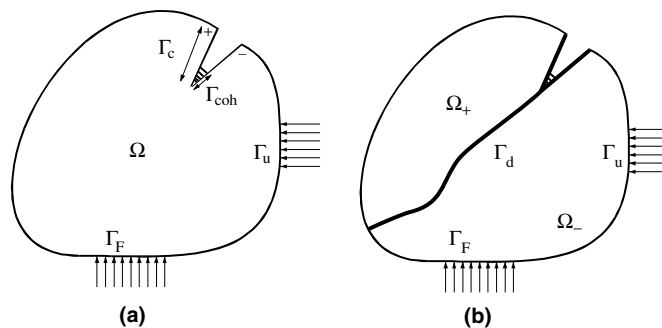

Fig. 2. Body Ω crossed by a material discontinuity Γ_d in the undeformed configuration.

The fundamental problem introduced by the interfacial surface Γ_d is how to express the virtual displacement jumps associated to the surfaces $\Gamma_{d^\pm}$ as a function of the virtual displacements. Consider a three-dimensional space with Cartesian coordinates X_i, $i = 1, 2, 3$. Let the Cartesian coordinates $x_i^\pm$ describe the position of the upper and lower surfaces $\Gamma_{d^\pm}$ in the deformed configuration. Considering Fig. 3, any material point on $\Gamma_{d^\pm}$ in the deformed configuration is related to its undeformed configuration through:

$$x_i^\pm = X_i + u_i^\pm \tag{5}$$

where $u_i^\pm$ are the displacements with respect to the fixed Cartesian coordinate system. The coordinates $\bar{x}_i$ of the midsurface can be written as (Ortiz and Pandolfi, 1999):

$$\bar{x}_i = X_i + \frac{1}{2}\left(u_i^+ + u_i^-\right) \tag{6}$$

The components of the displacement jump vector are evaluated at the midsurface $\overline{\Gamma}_d$, which is coincident with Γ_d in the undeformed configuration (see Fig. 3). The midsurface coordinate gradients define the components of the two vectors, v_{η_i} and v_{ξ_i}, that define the tangential plane at a given point, $\bar{P}$:

$$v_{\eta_i} = \bar{x}_{i,\eta} \tag{7}$$
$$v_{\xi_i} = \bar{x}_{i,\xi} \tag{8}$$

where η, ξ are curvilinear coordinates on the surface $\overline{\Gamma}_d$. Although v_{η_i} and v_{ξ_i} are generally not orthogonal to each other, their vector product defines a surface normal. Therefore, the local normal coordinate vector is obtained as

$$\mathbf{v}_n = \mathbf{v}_\xi \times \mathbf{v}_\eta \|\mathbf{v}_\xi \times \mathbf{v}_\eta\|^{-1} \tag{9}$$

The tangential coordinates are then obtained as

$$\mathbf{v}_s = \mathbf{v}_\xi \|\mathbf{v}_\xi\|^{-1} \tag{10}$$
$$\mathbf{v}_t = \mathbf{v}_n \times \mathbf{v}_s \tag{11}$$

The components of $\mathbf{v}_n$, $\mathbf{v}_s$ and $\mathbf{v}_t$ represent the direction cosines of the local coordinate system in the global coordinate system at a material point $\bar{P} \in \overline{\Gamma}_d$. The director cosines define an orthogonal rotation tensor Θ_{mi} relating the local coordinate system to the fixed coordinate system.

Using the rotation tensor, the normal and tangential components of the displacement jump tensor expressed in terms of the displacement field in global coordinates are:

$$\Delta_m = \Theta_{mi} [\![u_i]\!] \tag{12}$$

where Δ_m is the displacement jump tensor in the local coordinate system.

2.3. Constitutive laws

A constitutive law relating the cohesive tractions, τ_j, to the displacement jump in the local coordinates, Δ_i, is required for modeling the behavior of the material discontinuity. The constitutive laws in the material discontinuity may be formally written as

$$\tau_j = \tau(\Delta_i) \tag{13}$$
$$\dot{\tau}_j = D_{ji}^{\tan} \dot{\Delta}_i \tag{14}$$

where $D_{ji}^{\tan}$ is the constitutive tangent stiffness tensor.

A new constitutive model relating the displacement jumps to the tractions, and based on Damage Mechanics is proposed.

The delamination model proposed follows the general formulation of Continuum Damage Models
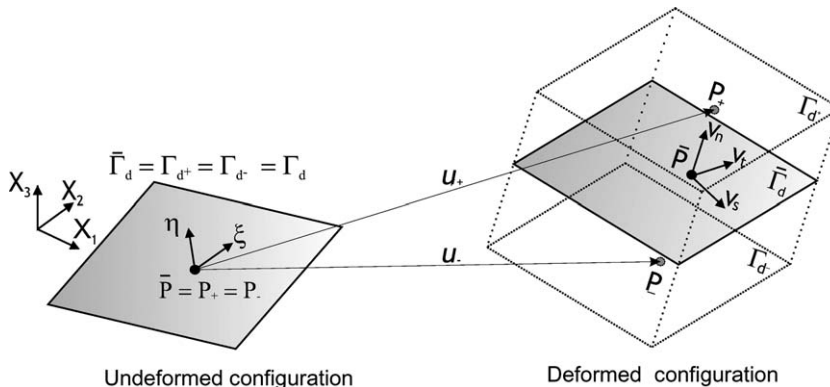

Fig. 3. Interfacial surface deformation.

proposed by Simo and Ju (1987a,b), and Mazars (1982).

The free energy per unit surface of the interface is defined as

$$\psi(\Delta, \mathsf{d}) = (1 - \mathsf{d})\psi^0(\Delta) \tag{15}$$

where d is a scalar damage variable, and ψ^0 is a convex function in the displacement jump space defined as

$$\psi^0(\Delta) = \frac{1}{2}\Delta_i D_{ij}^0 \Delta_j \quad i = 1,3; \ j = 1,3 \tag{16}$$

Negative values of Δ_3 do not have any physical meaning because interpenetration is prevented by contact. Therefore, a modification of Eq. (15) is proposed to prevent interfacial penetration of the two adjacent layers after complete decohesion. The expression for the free energy proposed is

$$\psi(\Delta, \mathsf{d}) = (1 - \mathsf{d})\psi^0(\Delta_i) - \mathsf{d}\psi^0(\overline{\delta}_{3i}\langle -\Delta_3 \rangle) \tag{17}$$

where $\langle \cdot \rangle$ is the MacAuley bracket defined as $\langle x \rangle = \frac{1}{2}(x + |x|)$ and $\overline{\delta}_{ij}$ is the Kronecker delta. The constitutive equation for the interface is obtained by differentiating the free energy with respect to the displacement jumps:

$$\tau_i = \frac{\partial \psi}{\partial \Delta_i} = (1 - \mathsf{d})D_{ij}^0 \Delta_j - \mathsf{d}D_{ij}^0 \overline{\delta}_{3j}\langle -\Delta_3 \rangle \tag{18}$$

The undamaged stiffness tensor, D_{ij}^0, is defined as

$$D_{ij}^0 = \overline{\delta}_{ij}K \tag{19}$$

where the scalar parameter K is a penalty stiffness. The constitutive equation can be written in Voigt notation as

$$\tau = \begin{Bmatrix} \tau_1 \\ \tau_2 \\ \tau_3 \end{Bmatrix} = (1 - \mathsf{d})K \begin{Bmatrix} \Delta_1 \\ \Delta_2 \\ \Delta_3 \end{Bmatrix} - \mathsf{d}K \begin{Bmatrix} 0 \\ 0 \\ \langle -\Delta_3 \rangle \end{Bmatrix} \tag{20}$$

The energy dissipation during damage evolution, Ξ, represented in Fig. 4 for single-mode loading, can be obtained from:

$$\Xi = -\frac{\partial \psi}{\partial \mathsf{d}}\dot{\mathsf{d}} \geqslant 0 \tag{21}$$

The model defined by Eq. (18) is fully determined if the value of the damage variable d is evaluated at every time step of the deformation process. For that purpose, it is necessary to define a suitable norm of the displacement jump tensor, a damage criterion, and a damage evolution law, as will be described in the following sections.
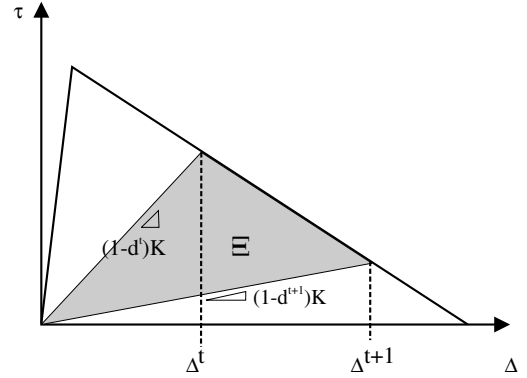

Fig. 4. Energy dissipation during damage evolution.

2.3.1. Norm of the displacement jump tensor

The norm of the displacement jump tensor is denoted as λ and is also called *equivalent displacement jump norm*. It is used to compare different stages of the displacement jump state so that it is possible to define such concepts as 'loading', 'unloading' and 'reloading'. The equivalent displacement jump is a non-negative and continuous function, defined as

$$\lambda = \sqrt{\langle \Delta_3 \rangle^2 + (\Delta_{\text{shear}})^2} \tag{22}$$

where Δ_3 is the displacement jump in mode I, i.e., normal to midplane, and Δ_{shear} is the Euclidean norm of the displacement jump in mode II and in mode III:

$$\Delta_{\text{shear}} = \sqrt{(\Delta_1)^2 + (\Delta_2)^2} \tag{23}$$

2.3.2. Damage criterion

The damage criterion is formulated in the displacement jump space. The form of this criterion is

$$F(\lambda^t, r^t) := \lambda^t - r^t \leqslant 0 \quad \forall t \geqslant 0 \tag{24}$$

where t indicates the actual time and r^t is the damage threshold for the current time. If r^0 denotes the initial damage threshold, then $r^t \geqslant r^0$ at every point in time. Damage initiation is produced when the displacement jump norm, λ, exceeds the initial damage threshold, r^0, which is a material property.

A fully equivalent expression for Eq. (24) that is more convenient for algorithmic treatment is (Oliver et al., 1990):

$$\overline{F}(\lambda^t, r^t) := \mathsf{G}(\lambda^t) - \mathsf{G}(r^t) \leqslant 0 \quad \forall t \geqslant 0 \tag{25}$$

where $\mathsf{G}(\cdot)$ is a suitable monotonic scalar function ranging from 0 to 1. $\mathsf{G}(\cdot)$ will define the evolution

of the damage value, and will be presented in the following section.

2.3.3. Damage evolution law

The evolution laws for the damage threshold and the damage variable must be defined in the damage model. These laws are defined by the rate expressions:

$$\dot{r} = \dot{\mu} \tag{26}$$

$$\dot{d} = \dot{\mu} \frac{\partial \overline{F}(\lambda, r)}{\partial \lambda} = \dot{\mu} \frac{\partial G(\lambda)}{\partial \lambda} \tag{27}$$

where $\dot{\mu}$ is a damage consistency parameter used to define loading–unloading conditions according to the Kuhn–Tucker relations:

$$\dot{\mu} \geqslant 0; \quad \overline{F}(\lambda^t, r^t) \leqslant 0; \quad \dot{\mu}\overline{F}(\lambda^t, r^t) = 0 \tag{28}$$

From the previous equations, it is easy to prove that the evolution of the internal variables can be integrated explicitly (Simo and Ju, 1987a):

$$r^t = \max\{r^0, \max_s \lambda^s\} \quad 0 \leqslant s \leqslant t \tag{29}$$

$$d^t = G(r^t) \tag{30}$$

which fully describes evolution of the internal variables for any loading–unloading–reloading situation. The scalar function $G(\cdot)$ defines the evolution of the damage value. For a given mixed-mode ratio, β, the function proposed here is defined as

$$G(\lambda) = \frac{\Delta^f(\lambda - \Delta^0)}{\lambda(\Delta^f - \Delta^0)} \tag{31}$$

Eq. (31) defines the damage evolution law by means of a bilinear constitutive equation (see Fig. 5), where Δ^0 is the onset displacement jump, and it is equal to the initial damage threshold r^0. The initial damage

Fig. 5. A bilinear constitutive equation for the decohesion element for a mixed-mode loading situation.

threshold is obtained from the formulation of the initial damage surface or initial damage criterion. Δ^f is the final displacement jump, and it is obtained from the formulation of the propagation surface or propagation criterion.

It is therefore necessary to establish the delamination onset and propagation surfaces for the complete definition of the damage model. Delamination onset and propagation surfaces and the damage evolution law fully define the constitutive equations.

The constitutive equations for the interfacial surface are normally developed in a phenomenological way, i.e., satisfying empirical relations that are obtained using experimental results. There are several types of constitutive equations used in decohesion elements: Tvergaard and Hutchinson (1992) proposed a trapezoidal law, Cui and Wisnom (1993) a perfectly plastic rule, Needleman first proposed a polynomial law (Needleman, 1987) and later an exponential law (Xu and Needleman, 1994). Goyal-Singhal et al. (2002) adopted Needleman's exponential law to account for load reversal without restoration of the cohesive state.

The law proposed here is a bilinear relation between the tractions and the displacement jumps (Mi et al., 1998; Camanho et al., 2003; Reddy et al., 1997). The bilinear law is the most commonly used cohesive law due to its simplicity. One drawback of the bilinear law is that the traction–displacement jump relation is discontinuous at the peak value of the traction. The discontinuity in the traction–displacement jump relation can be avoided using continuous functions. However, even for such continuous functions, the discontinuity is unavoidable when modeling loading–unloading cycles.

For a given mixed-mode ratio, β, defined as

$$\beta = \frac{\Delta_{\text{shear}}}{\Delta_{\text{shear}} + \langle \Delta_3 \rangle} \tag{32}$$

the bilinear constitutive equation is defined by a penalty parameter, K, the damage value, d, the mixed-mode damage initiation, Δ^0, and the total decohesion parameter, Δ^f. These last two values are given by the formulation of the onset and the propagation criterion which takes into account the interaction between different modes, and their value depends on the mixed-mode ratio β. The penalty parameter K assures a stiff connection between two neighboring layers before delamination initiation. The penalty parameter should be large enough to provide a reasonable stiffness but small enough to avoid numerical problems, such as spurious traction
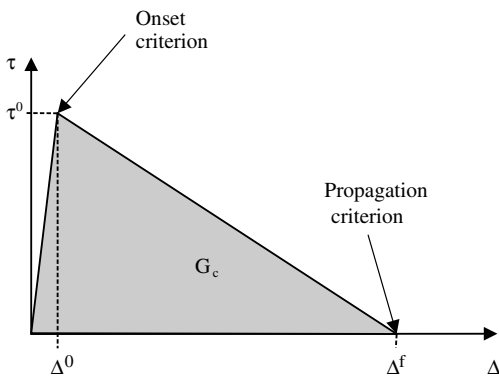
oscillations (Schellekens and de Borst, 1992), in a finite element analysis.

2.3.4. Propagation criterion

The criteria used to predict delamination propagation under mixed-mode loading conditions are usually established in terms of the components of the energy release rate and fracture toughness. It is assumed that when the energy release rate, G, exceeds the critical value, the critical energy release rate G_c, delamination grows.

The most widely used criterion to predict delamination propagation under mixed-mode loading, the "power law criterion" is normally established in terms of a linear or quadratic interaction between the energy release rates (Wu and Reuter, 1965). However, Camanho et al. (2003) have shown that the expression proposed by Benzeggagh and Kenane (1996) for the critical energy release rate for a mixed-mode ratio is more accurate for epoxy and PEEK composites. The expression proposed by Benzeggagh and Kenane for the critical energy release rate G_c is

$$G_c = G_{Ic} + (G_{IIc} - G_{Ic})\left(\frac{G_{shear}}{G_T}\right)^{\eta} \tag{33}$$

Delamination growth is produced when the total energy release rate G is greater or equal than the critical value G_c:

$$G \geqslant G_c \tag{34}$$

The energy release rate under mixed-mode loading is $G = G_I + G_{shear}$ where $G_{shear} = G_{II} + G_{III}$ is the energy release rate for shear loading proposed by Li and Sen (2000) and Li (2000).

The propagation surface in the displacement jump space is defined through the final displacements, which are obtained from the pure mode fracture toughness (G_{Ic}, G_{IIc}, G_{IIIc}) considering that the area under the traction–displacement jump curves is equal to the corresponding fracture toughness, i.e.

$$G_c = \frac{1}{2}K\Delta^0\Delta^f \tag{35}$$

Using Eq. (35) in Eq. (33) the propagation criterion is obtained in the displacement jump space as

$$\Delta^f = \frac{\Delta_3^0\Delta_3^f + \left(\Delta_{shear}^0\Delta_{shear}^f - \Delta_3^0\Delta_3^f\right)\left(\frac{G_{shear}}{G_T}\right)^{\eta}}{\Delta^0} \tag{36}$$

where Δ_3^0 and Δ_{shear}^0 are the pure mode onset displacement jumps and Δ_3^f and Δ_{shear}^f are the pure

mode final displacement jumps. It is necessary to obtain the ratio $\frac{G_{shear}}{G_T}$ to fully define the final displacement jump. For a given mixed-mode ratio, β, the energy release rates are obtained from:

$$G_I = \frac{1}{2}K\left(\Delta_3^0(\beta)\Delta_3^f(\beta) - \Delta_3\Delta_3^f(\beta)\right) \tag{37}$$

$$G_{shear} = \frac{1}{2}K\left(\Delta_{shear}^0(\beta)\Delta_{shear}^f(\beta) - \Delta_{shear}\Delta_{shear}^f(\beta)\right) \tag{38}$$

where $\Delta_{shear}^0(\beta)$ and $\Delta_3^0(\beta)$ are respectively the shear and normal displacement jumps corresponding to the onset of softening under mixed-mode loading, $\Delta_{shear}^f(\beta)$ and $\Delta_3^f(\beta)$ are the shear and normal displacement jumps corresponding to the total decohesion under mixed-mode loading, and Δ_{shear} and Δ_3 are the components of the current displacement jump.

From (32)

$$\Delta_{shear}^0(\beta) = \Delta_3^0(\beta)\frac{\beta}{1-\beta} \tag{39}$$

$$\Delta_{shear}^f(\beta) = \Delta_3^f(\beta)\frac{\beta}{1-\beta} \tag{40}$$

$$\Delta_{shear} = \Delta_3\frac{\beta}{1-\beta} \tag{41}$$

Using Eqs. (39)–(41) in (37) and (38), the ratio between $\frac{G_{shear}}{G_T}$ can be established in terms of β. Since the ratio $\frac{G_{shear}}{G_T}$ is only a function of the mixed-mode ratio β, henceforward this ratio is named as B:

$$B = \frac{G_{shear}}{G_T} = \frac{\beta^2}{1 + 2\beta^2 - 2\beta} \tag{42}$$

2.3.5. Initial damage surface

Under pure mode I, mode II or mode III loading, delamination onset occurs when the corresponding interlaminar traction exceeds its respective maximum interfacial strength, $\tau_3^0, \tau_2^0, \tau_1^0$. Under mixed-mode loading, an interaction between modes must be taken into account. Few models take into account the interaction of the traction components in the prediction of damage onset. The models that account for the interaction of the traction components are usually based on Ye's criterion (Ye, 1988), using a quadratic interaction of the tractions:

$$\left(\frac{\langle\tau_3\rangle}{\tau_3^0}\right)^2 + \left(\frac{\tau_2}{\tau_2^0}\right)^2 + \left(\frac{\tau_1}{\tau_1^0}\right)^2 = 1 \tag{43}$$

However, experimental data for the initiation of delamination under mixed-mode is not readily available and, consequently, failure criteria that

can predict the initiation have not been fully validated.

The criterion for propagation is often formulated independently of the criterion for initiation. In this paper, a link between propagation and initiation is proposed. Since delamination is a fracture process, the initiation criterion proposed in this paper evolves from the propagation criterion and the damage evolution law. The isodamage surface for a damage value equal to 1 corresponds to the propagation surface obtained from Eq. (33). Then, the isodamage surface for a damage value equal to 0 is the initial damage surface. With these assumptions, the criterion for delamination initiation proposed here is

$$(\tau^0)^2 = (\tau_3)^2 + (\tau_1)^2 + (\tau_2)^2$$
$$= (\tau_3^0)^2 + \left(\left(\tau_{shear}^0\right)^2 - \left(\tau_3^0\right)^2 \right) B^\eta \qquad (44)$$

In the displacement jump space, the criterion becomes:

$$(\Delta^0)^2 = (\Delta_3)^2 + (\Delta_1)^2 + (\Delta_2)^2$$
$$= (\Delta_3^0)^2 + \left(\left(\Delta_{shear}^0\right)^2 - \left(\Delta_3^0\right)^2 \right) B^\eta \qquad (45)$$

The initiation criterion developed here and summarized by Eq. (44) is compared with Ye's criterion, given by Eq. (43), and with a maximum traction criterion that does not take into account interaction between the tractions. The surfaces obtained by the different criteria are represented in Fig. 6 for AS4/PEEK carbon-fiber-reinforced composite. The material properties used are summarized in Table 1. The parameter $\eta = 2.284$ was obtained applying a least-squares fit to the experimental data shown in Table 2 (Camanho et al., 2003). The predictions of the new criterion are very close to the ones obtained using Ye's criterion, which has been successfully used in previous investigations (Camanho et al., 2003).

The formulation presented assures a smooth transition for all mixed-mode ratios between the initial damage surface to the propagation surface through damage evolution. If the loading mode changes, the formulation presented avoids the restoration of the cohesive state and assures that the energy dissipation is always positive.

The evolution of the damage surface from the damage initiation surface to the propagation surface is represented in Fig. 7, for positive values of displacement jumps.

2.4. Formulation of the constitutive tangent tensor

The constitutive tangent tensor needs to be defined for the numerical implementation of the proposed model. The constitutive tangent tensor is
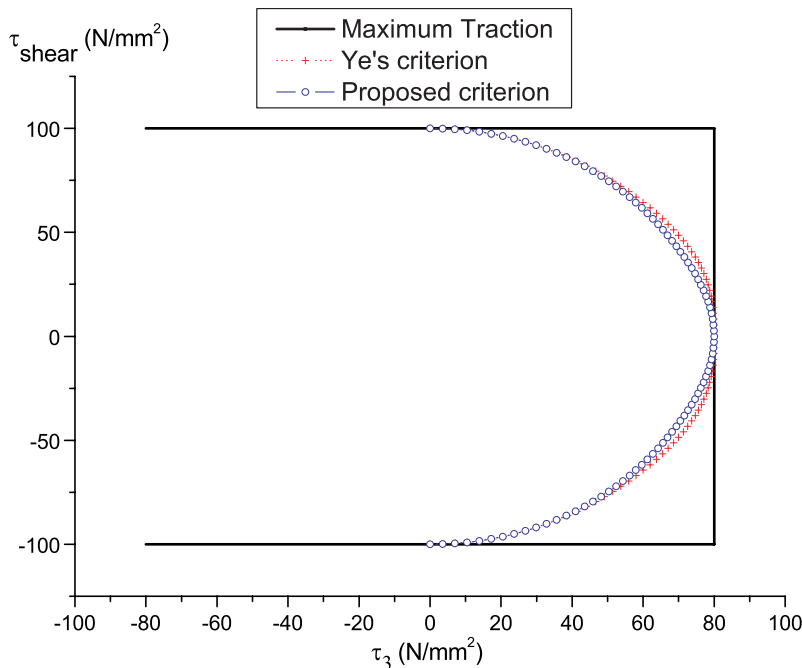

Fig. 6. Comparison between Ye's criterion, a maximum traction criterion and the new proposed criterion.

Table 1
Material properties for AS4/PEEK carbon-fiber-reinforced composite

E_{11}	$E_{22} = E_{33}$	$G_{12} = G_{13}$	G_{23}	$v_{12} = v_{13}$	v_{23}	G_{Ic}	G_{IIc}	τ_3^0	$\tau_2^0 = \tau_1^0$
122.7 GPa	10.1 GPa	5.5 GPa	3.7 GPa	0.25	0.45	0.969 kJ/m²	1.719 kJ/m²	80 MPa	100 MPa

Table 2
Experimental data

	G_{II}/G_T				
	0% (DCB)	20%	50%	80%	100% (ENF)
G_c (kJ/m²)	0.969		1.103	1.131	1.376	1.719
a_0 (mm)	32.9		33.7	34.1	31.4	39.2

obtained from the differentiation of the secant equation (18):

$$\dot{\tau}_i = D_{ij}\dot{\Delta}_j - \overline{\delta}_{ij}K\left[1 + \overline{\delta}_{3j}\frac{\langle -\Delta_j\rangle}{\Delta_j}\right]\Delta_j\dot{d} \tag{46}$$

where D_{ij} is defined as

$$D_{ij} = \overline{\delta}_{ij}K\left[1 - d\left(1 + \overline{\delta}_{3j}\frac{\langle -\Delta_j\rangle}{\Delta_j}\right)\right] \tag{47}$$

The evolution of the damage variable d only occurs for loading situations. Therefore, the evolution of the damage variable can be written as

$$\dot{d} = \begin{cases} \dot{G}(\lambda) = \frac{\partial G(\lambda)}{\partial\lambda}\dot{\lambda}, & r < \lambda < \Delta^f \\ 0, & r > \lambda \text{ or } \Delta^f < \lambda \end{cases} \tag{48}$$

where the variation of the function G is obtained assuming that the variation of the final displacement jump Δ^f and the onset displacement jump Δ^0 with the mixed-mode ratio β are not significant for the time increment taken:

$$\frac{\partial G(\lambda)}{\partial\lambda} = \frac{\Delta^f \Delta^0}{\Delta^f - \Delta^0}\frac{1}{\lambda^2} \tag{49}$$

The evolution of the displacement norm is obtained from Eq. (22):

$$\dot{\lambda} = \frac{\partial\lambda}{\partial\Delta_k}\dot{\Delta}_k = \frac{\Delta_k}{\lambda}\left(1 + \overline{\delta}_{3k}\frac{\langle -\Delta_k\rangle}{\Delta_k}\right)\dot{\Delta}_k \tag{50}$$

Using Eq. (48) through (50), Eq. (46) can be written as

$$\dot{\tau}_i = D_{ij}^{\tan}\dot{\Delta}_j \tag{51}$$

$$D_{ij}^{\tan} = \begin{cases} \left\{D_{ij} - K\left[1 + \overline{\delta}_{3j}\frac{\langle -\Delta_j\rangle}{\Delta_j}\right]\left[1 + \overline{\delta}_{3i}\frac{\langle -\Delta_i\rangle}{\Delta_i}\right]H\Delta_i\Delta_j\right\}, \\ \qquad r < \lambda < \Delta^f \\ D_{ij}, \quad r > \lambda \text{ or } \Delta^f < \lambda \end{cases} \tag{52}$$

where H is a scalar value given by

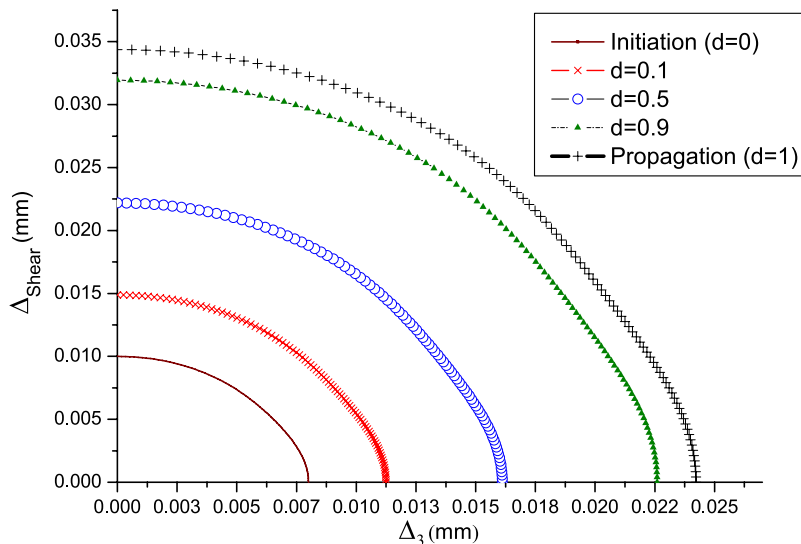$$H = \frac{\Delta^f \Delta^0}{\Delta^f - \Delta^0}\frac{1}{\lambda^3} \tag{53}$$

Fig. 7. Damage evolution surface in the relative displacements space.

3. Finite element discretization—computational model

To transform the strong form of the boundary value problem into a weak form better suited for finite element computations, the velocities v_i must belong to the set $\mathscr{U}$ of the kinematically admissible velocity field which allows for discontinuous velocities across the boundary Γ_d of the delamination.

The spaces for the test functions and trial functions are defined as

$$\delta v_i(\mathbf{X}) \in \mathscr{U}_0, \quad \mathscr{U}_0 = \{\delta v_i | \delta v_i \in C^0(\mathbf{X}), \delta v_i = 0 \text{ on } \Gamma_{v_i}\} \tag{54}$$

$$v_i(\mathbf{X}, t) \in \mathscr{U}, \quad \mathscr{U} = \{v_i | v_i \in C^0(\mathbf{X}), v_i = \overline{v}_i \text{ on } \Gamma_{v_i}\} \tag{55}$$

The space of velocities in $\mathscr{U}$ are the kinematically admissible velocities or compatible velocities. The space $\mathscr{U}$ satisfies the continuity conditions required for compatibility and the displacement boundary conditions.

Considering Fig. 2, the weak form of the momentum equation is obtained as

$$\sum_{\Omega_\pm} \int_{\Omega_\pm} \left(\frac{\partial \sigma_{ij}}{\partial x_j} + \rho b_i \right) \delta v_i \, \mathrm{d}\Omega_\pm = 0 \quad \forall v_i \in \mathscr{U} \tag{56}$$

where b_i are the body forces and ρ is the density of the material.

Using the decomposition of the velocity gradient and the traction continuity condition, the weak form of the momentum equation in an updated Lagrangian formulation is obtained as

$$\int_{\Gamma_d} t_i \delta[\![v_i]\!] \, \mathrm{d}\Gamma_d + \sum_{\Omega_\pm} \int_{\Omega_\pm} \delta D_{ij} \sigma_{ij} \, \mathrm{d}\Omega_\pm$$
$$= \sum_{\Gamma_\pm} \int_{\Gamma_\pm} n_j (\delta v_i \sigma_{ji}) \, \mathrm{d}\Gamma_\pm$$
$$+ \sum_{\Omega_\pm} \int_{\Omega_\pm} \delta v_i \rho b_i \, \mathrm{d}\Omega_\pm \quad \forall v_i \in \mathscr{U} \tag{57}$$

where t_i is the traction tensor, σ_{ij} is the Cauchy stress tensor, and D_{ij} is the rate of deformation tensor. From Eq. (57), it is clear that the tractions occurring at the cohesive interface are work-conjugate with the displacement jumps.

The discretization of the domain is performed by the discretization of the whole domain Ω with standard volume elements. However, the surfaces surrounding the potential delamination Γ_d are discretized with decohesion elements (Camanho et al., 2003). The discretized formulation is divided in the two domains considering no formal coupling between the continuous and the discontinuous parts of the deformation in the expression for the free energy of the interface (Larsson and Jansson, 2002).

3.1. Discretization of the interfacial surface

The displacements and displacement gradients for the decohesion elements are approximated as

$$u_i|_{\Omega_e} = N_K^e q_{Ki}^e \tag{58}$$

$$[\![u_i]\!]|_{\Omega_e} = \overline{N}_K^e q_{Ki}^e \tag{59}$$

with

$$\overline{N}_K^e = \begin{cases} N_K^e & K \in \Gamma_d^+ \\ -N_K^e & K \in \Gamma_d^- \end{cases} \tag{60}$$

where q_{Ki}^e is the displacement in the i direction of the K node of the element e, N_K^e are standard Lagrangian shape functions (Belytschko et al., 2001). $\overline{N}_K^e$ are Lagrangian shape functions defined for the decohesion elements (Camanho et al., 2003).

According to Eq. (58), the displacement field, u_i, and the undeformed material coordinate, X_i, associated with the surfaces $\Gamma_{d\pm}$ are interpolated as follows:

$$u_i^\pm = N_K q_{Ki}^\pm \tag{61}$$

$$X_i^\pm = N_K p_{Ki}^\pm \tag{62}$$

where $q_{Ki}^\pm$ are the nodal displacement vectors and $p_{Ki}^\pm$ are the undeformed material nodal coordinate vectors. Note that the values of p_{Ki}^- and p_{Ki}^+ can be different in the case that an initial crack exists. Using these equations, the material coordinates of the interfacial midsurface are:

$$\overline{x}_i = \frac{1}{2} N_K (p_{Ki}^+ + p_{Ki}^- + q_{Ki}^+ + q_{Ki}^-) \tag{63}$$

The components of the two vectors that define the tangential plane can be written as

$$v_{\eta_i} = \overline{x}_{i,\eta} = N_{K,\eta} \frac{1}{2} (p_{Ki}^+ + p_{Ki}^- + q_{Ki}^+ + q_{Ki}^-) \tag{64}$$

$$v_{\xi_i} = \overline{x}_{i,\xi} = N_{K,\xi} \frac{1}{2} (p_{Ki}^+ + p_{Ki}^- + q_{Ki}^+ + q_{Ki}^-) \tag{65}$$

Using (59) and (12), the displacement jump can then be obtained in local coordinates as

$$\Delta_m = \Theta_{im} \overline{N}_K q_{Ki} = \overline{B}_{imK} q_{Ki} \tag{66}$$

The contribution of a decohesion element for the internal load vector is given by

$$f_{iK}^{\text{int}} = \int_{\Gamma_d} \tau_n \overline{B}_{inK} \, d\Gamma_d \tag{67}$$

with $\overline{B}_{inK} = \Theta_{in}\overline{N}_K^e$.

The softening nature of the decohesion element constitutive equation causes difficulties in obtaining a converged solution for the non-linear problem when using Newton–Raphson iterative method. In particular, quadratic convergence is not assured because the residual vector is not continuously differentiable with respect to the nodal displacements.

The tangent stiffness matrix stems from the linearization of the internal force vector and it is obtained using Taylor's series expansion about the approximation q_{Ki} (Goyal-Singhal et al., 2004). Taking into account that the calculation of the geometric terms of the tangent stiffness matrix is computationally very intensive, these terms are neglected. The tangent stiffness matrix, K_{rZiK}, for the decohesion element is therefore approximated as

$$K_{rZiK} \approx \int_{\Gamma_d} \overline{B}_{jrZ} D_{nj}^{\text{tan}} \overline{B}_{inK} \, d\Gamma_d \tag{68}$$

where D_{ij}^{tan} is the material tangent stiffness matrix, or constitutive tangent tensor defined in Section 2.4.

4. Comparison with experimental studies

The formulation proposed here was implemented in the ABAQUS Finite Element code (Anon., 1996) as a user-written element subroutine (UEL).

To verify the element under different loading conditions, the numerical predictions were compared with experimental data obtained for composite test specimens and aircraft subcomponents. The double cantilever beam (DCB) test, the end notched flexure (ENF) test, and mixed-mode bending (MMB) tests in PEEK/AS4, a thermoplastic matrix composite material, were simulated.

The debonding of a composite co-cured skin-stiffener subcomponent loaded under tension was simulated, and the numerical results were compared with experimental data.

4.1. Mode I, mode II and mixed-mode I and II delamination growth for a PEEK composite

The most widely used specimen for mixed-mode fracture is the mixed-mode bending (MMB) specimen shown in Fig. 8, which was proposed by Crews and Reeder (1988), Reeder and Crews (1990) and Reeder and Crews (1991).
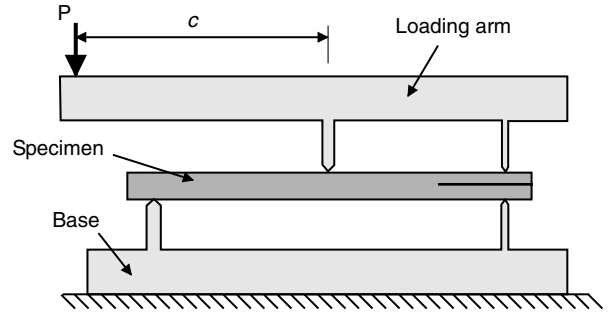

Fig. 8. MMB test specimen.

The main advantages of the MMB test method are the possibility of using virtually the same specimen configuration as for mode I tests, and the capability of obtaining different mixed-mode ratios, ranging from pure mode I to pure mode II, by changing the length c of the loading lever shown in Fig. 8.

An 8-node decohesion element is used to simulate DCB, ENF and MMB tests in unidirectional AS4/PEEK carbon-fiber-reinforced composite. The specimens simulated are 102-mm-long, 25.4-mm-wide, with two 1.56-mm-thick arms. The material properties are shown in Table 1, and a stiffness $K = 10^6$ N/mm^3 is used.

The experiments used to assess the accuracy of the model proposed were performed by Crews and Reeder (1988), Reeder and Crews (1990) and Reeder and Crews (1991). The experimental tests were performed at different $\frac{G_{II}}{G_T}$ ratios, ranging from pure mode I loading to pure mode II loading. The initial delamination length of the specimens (a_0) and the mixed-mode fracture toughness obtained experimentally are shown in Table 2.

Models using 150 decohesion elements along the length of the specimens, and 4 decohesion elements along the width, were created to simulate the ENF and MMB test cases. The initial size of the delamination is simulated by placing open decohesion elements along the length corresponding to the initial delamination of each specimen (see Table 2). These elements are capable of dealing with the contact conditions occurring for mode II or mixed-mode I and II loading, therefore avoiding interpenetration of the delamination faces. The model of the DCB test specimen uses 102 decohesion elements along the length of the specimen.

The different G_{II}/G_I ratios are simulated by applying different loads at the middle and at the end of the test specimen. The analytical determination of

the middle and end loads for each mode ratio is presented in Camanho et al. (2003).

The experimental results relate the load to the displacement of the point of application of the load P in the lever (load-point displacement, Fig. 8). Since the lever is not simulated, it is necessary to determine the load-point displacement from the displacement at the end and at the middle of the spec-imen using the analytical procedure described in (Camanho et al., 2003).

The B-K parameter, $\eta = 2.284$, is calculated by applying a least-squares fit to the experimental data shown in Table 2.

The numerical predictions and the experimental data for all the test cases simulated are shown in Figs. 9–13.
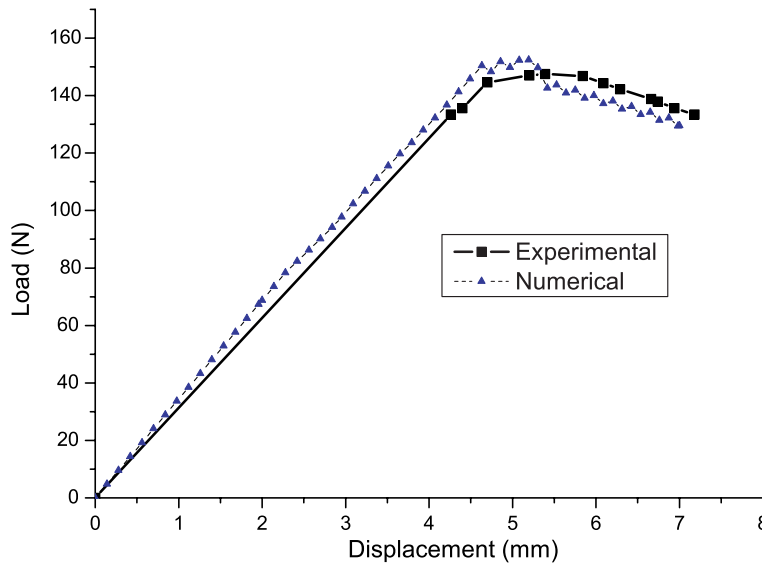
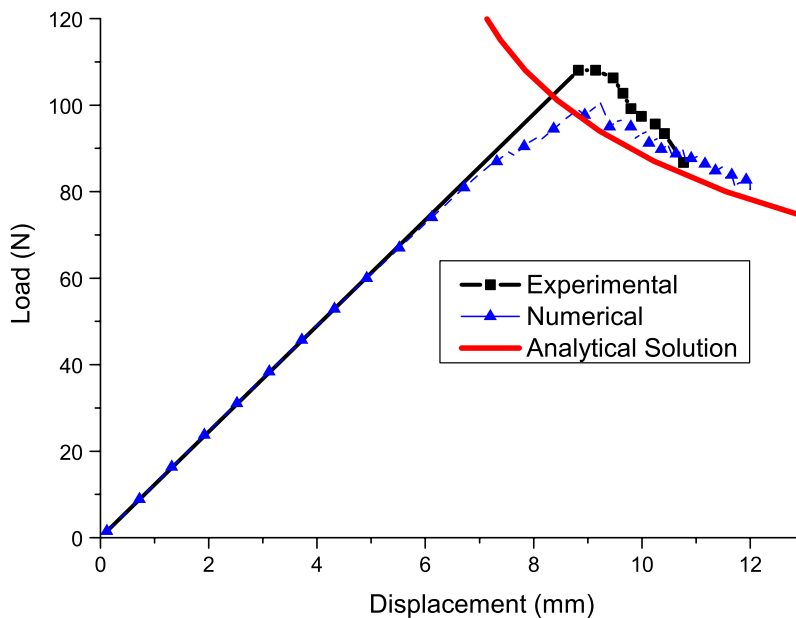Fig. 9. Numerical and experimental results—pure mode I loading.

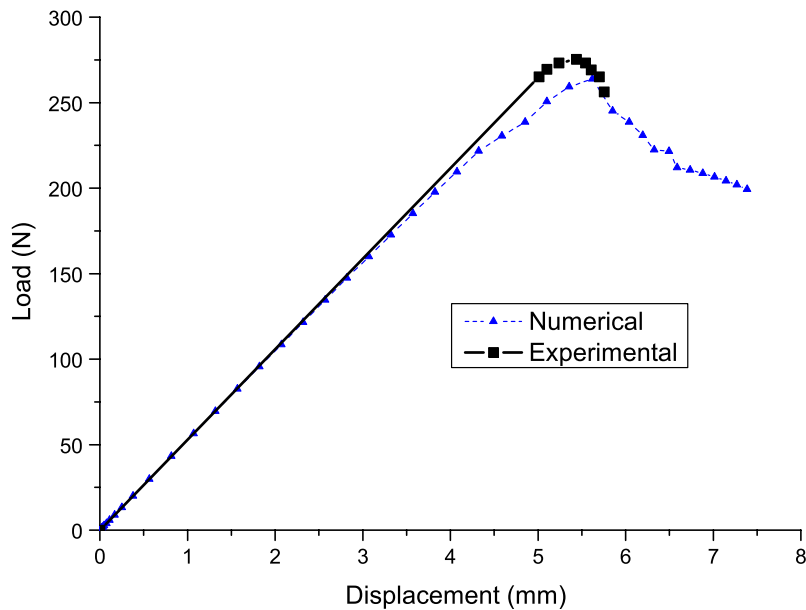Fig. 10. Numerical and experimental results—mixed-mode I and II loading with $G_{II}/G_T = 20\%$.

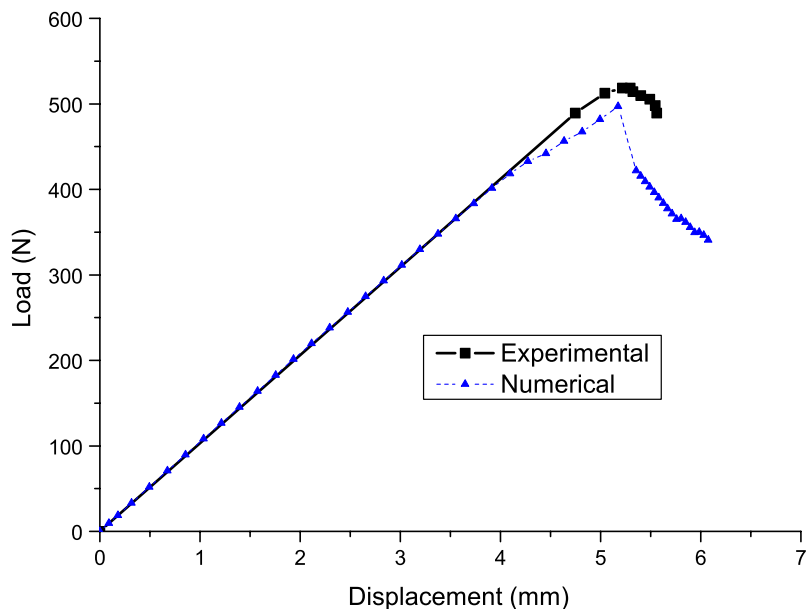Fig. 11. Numerical and experimental results—mixed-mode I and II loading with $G_{II}/G_T = 50\%$.

Fig. 12. Numerical and experimental results—mixed-mode I and II loading with $G_{II}/G_T = 80\%$.

A comparison of the results shown in Table 3 indicates good correlation between the predicted maximum loads and the experimental results. The largest difference (-7.0%) corresponds to the case of an MMB test specimen with $\frac{G_{II}}{G_T} = 20\%$ (Fig. 10). This difference is not due to limitations with the analytical procedure but rather with the B-K curve fit of the measured toughness. The largest error corresponds to $\frac{G_{II}}{G_T} = 20\%$, where the experimental fracture toughness is 1.103 kJ/m^2 whereas the B-K curve fit is 0.988 kJ/m^2 (Camanho et al., 2003).

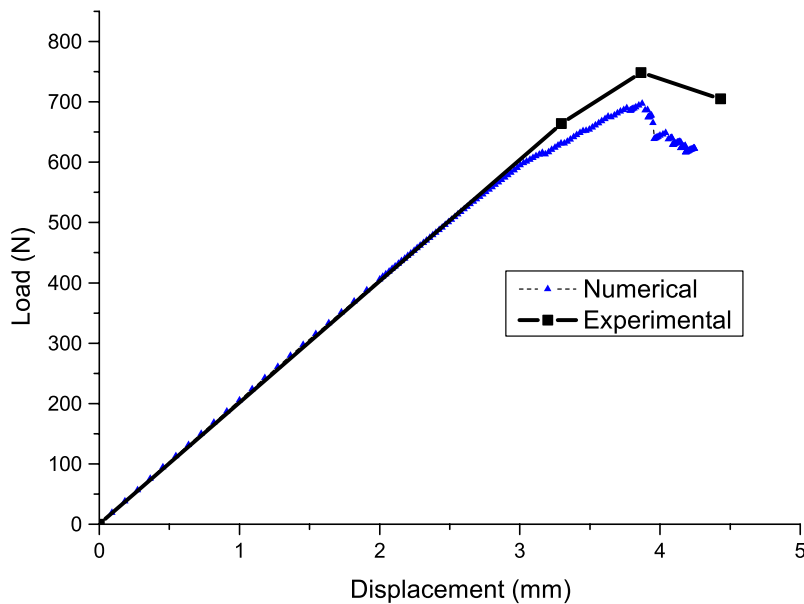Mi and Crisfield (1996) fracture propagation analytical model is shown in Fig. 10 for the MMB

Fig. 13. Numerical and experimental results—pure mode II loading.

Table 3
Experimental and predicted maximum loads for AS4/PEEK DCB, MMB and ENF specimens

G_{II}/G_T	Predicted (N)	Experimental (N)	Error (%)
0% (DCB)	152.4	147.5	3.4
20% (MMB)	100.5	108.1	−7.0
50% (MMB)	263.9	275.3	−4.2
80% (MMB)	496.9	518.7	−4.2
100% (ENF)	697.1	748.4	−6.9

test specimen with $\frac{G_{II}}{G_T} = 20\%$ and for a fracture toughness $G_c = 0.988$ kJ/m^2. Fig. 10 shows an excellent correlation between the descending part of the analytical load–displacement curve and the numerical prediction. Such comparison cannot be made with the results in Figs. 11–13 because too few data points were recorded during the propagation phases of those tests.

4.2. Skin-stiffener co-cured structure

Most composite components in aerospace structures are made of panels with co-cured or adhesively bonded frames and stiffeners. Testing of stiffened panels has shown that bond failure at the tip of the stiffener flange is a common failure mode. Comparatively simple specimens consisting of a stringer flange bonded onto a skin have been developed by Krueger et al. to study skin/stiffener debonding

(Krueger et al., 2000). The configuration of the specimens studied by Krueger is shown in Fig. 14.

The specimens are 203-mm-long, 25.4-mm-wide. Both skin and flange were made from IM6/3501-6 graphite/epoxy prepreg tape with a nominal ply thickness of 0.188 mm. The skin lay-up consisting of 14 plies was $(0°/45°/90°/−45°/45°/−45°/0°)_S$ and the flange lay-up consisting of 10 plies was $(45°/90°/−45°/0°/90°)_S$.

The properties of the unidirectional graphite/epoxy and the properties of the interface reported in Krueger et al. (2000) are shown in Tables 4 and 5, respectively.
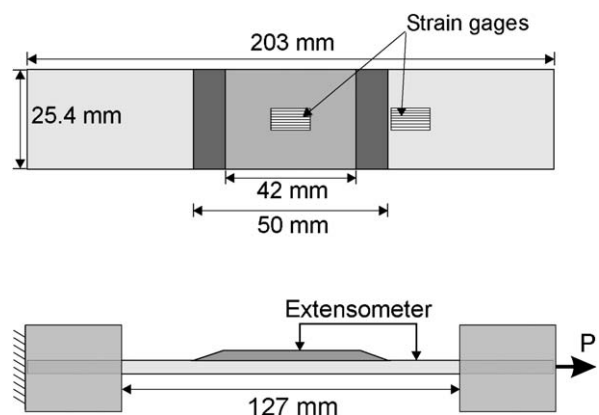

Fig. 14. Skin-stiffener test specimen.

Table 4

Material properties for IM6-3501-6 unidirectional graphite epoxy

E_1 (GPa)	$E_2 = E_3$ (GPa)	$v_{12} = v_{13}$	v_{23}	$G_{12} = G_{13}$ (GPa)	G_{23} (GPa)
144.7	9.6	0.3	0.45	5.2	3.4

Table 5

Properties of the interface (IM6/3501-6 unidirectional graphite/epoxy)

G_{Ic} (kJ/m^2)	G_{IIc} (kJ/m^2)	N (MPa)	S (MPa)	η
0.075	0.547	61	68	1.45

The parameter for the B-K criterion is taken from test data for IM6/3501-625 as $\eta = 1.45$, and a stiffness $K = 10^6 \text{ N/mm}^3$ is used. It should be noted that the model developed accounts for mode III loading by using the concept of shear component of the energy release rate, $G_{shear} = G_{II} + G_{III}$, and by assuming $G_{IIc} = G_{IIIc}$.

To keep the modeling difficulties low and the approach applicable to larger problems, the model that was developed uses only two brick elements through the thickness of the skin, and another two through the flange. Unsymmetric layered properties were assigned to the three-dimensional elements by using the composite solid section option in ABAQUS. This option calculates the element's stiffness by performing a Simpson's integration through the thickness using material points in each of the plies within the element. Approximations were necessary in the tapered sections of the flange because planes of integration cannot be defined parallel to the plies in the tapered elements. Additional details on the model can be found in Dávila et al. (2001).

The complete model consists of 1002 three-dimensional 8-node C3D8I laminated solid elements that allow non-symmetric lay-up (Anon., 1996), and 15,212 degrees of freedom (Camanho et al., 2004). To prevent delamination from occurring at both ends of the flange simultaneously, model symmetry was reduced by modeling the tapered end of the flange with a refined mesh on one side and a coarser mesh on the other. Unlike the previous examples, this model does not contain any pre-existing delaminations.

Residual thermal effects in the composite plies are simulated by performing a thermal analysis step before the mechanical loads are applied. The same coefficients of thermal expansion ($\alpha_{11} = -2.4 \times 10^{-8}/°\text{C}$ and $\alpha_{22} = 3.7 \times 10^{-5}/°\text{C}$) are applied to the skin and the flange, and the temperature difference between the room and curing temperatures is $\Delta T = -157 °\text{C}$. The flange has more 90° plies than $0°$ plies, and the skin is quasi-orthotropic, so it is expected that residual thermal stresses are present at their interface at room temperature.

Deformed plots of the finite element model immediately before and after flange separation are shown in Fig. 15.

It can be observed that only the refined end of the flange separates. It is worth noticing that the debond growth is not symmetric across the width: the debond initiates on the left corner of the flange shown on the bottom left of Fig. 15 due to the lack of symmetry introduced by the terminated plies at the flange tapered ends. This behavior was also observed in the experiments (Krueger et al., 2000).

Fig. 16 shows the load–extensometer measurement relation obtained in four experiments and the corresponding numerical prediction. Debond is detected in the experiments by the discontinuities in the load–displacement relation, and in the numerical simulation when the delamination propagates along the width of the specimen.

Table 6 compares the average of the measured debond loads with the numerical predictions.

It can be observed that good accuracy in the prediction of the debond loads is obtained. The predicted stiffness of the specimen is also in good agreement with the experimental data. The stiffening
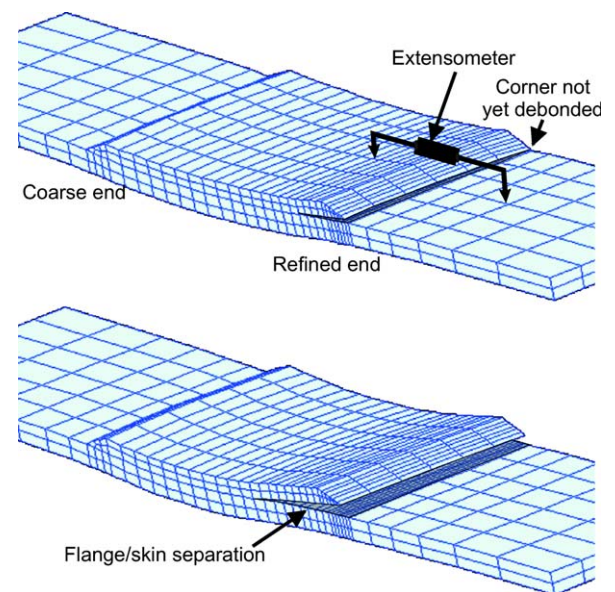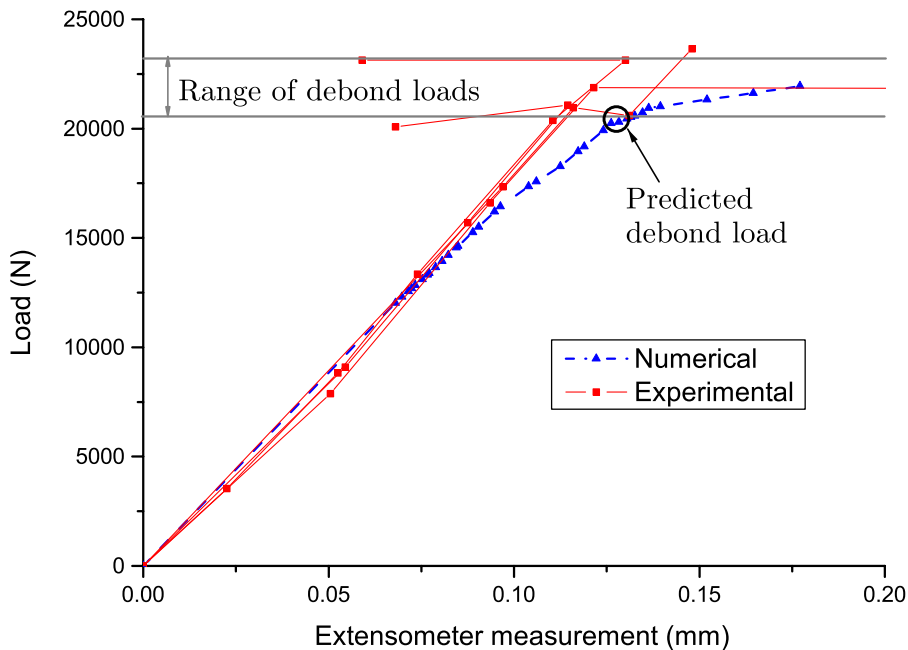

Fig. 15. Skin-stiffener debonding.

Fig. 16. Experimental and numerical load–extensometer displacement relations.

Table 6
Comparison between experimental and numerical results

	Experimental (kN)	Predicted (kN)	Error (%)
Flange debond load	21.7 ± 1	19.9	−8.3

effect detected in the experiments, Fig. 16, is due to the extensometer rotation as a result of specimen bending. Although specimen bending is properly represented by the numerical model, the extensometer measurement calculated from the numerical model does not account for the rotation of the extensometer.

5. Concluding remarks

A thermodynamically consistent model for the simulation of progressive delamination based on Damage Mechanics was presented. A constitutive equation for the interface was derived from the free energy of the interface. The resulting damage model simulates delamination onset and delamination propagation. The constitutive equation proposed uses a single scalar variable to track the damage at the interface under general loading conditions. A new initiation criterion that evolves from the Benzeggagh–Kenane propagation criterion has been developed to assure that the model accounts for changes in the loading mode in a thermodynamically consistent way and avoids restoration of the cohesive state. The damage model was implemented in a finite element model. The material properties required to define the element constitutive equations are the interlaminar fracture toughnesses, the penalty stiffness, and the strengths of the interface. In addition, a material parameter η, which is determined from standard delamination tests, is required for the Benzeggagh–Kenane mode interaction law.

Two examples were presented that test the accuracy of the method. In the first example, the simulations of the DCB, ENF and MMB tests represent cases of single-mode and mixed-model delamination. A composite skin-stiffener co-cured sub-component was also simulated, and the model predictions were compared with available experimental data.

The examples analyzed are in good agreement with the test results, and they indicate that the proposed formulation can predict the strength of composite structures that exhibit progressive delamination.

References

Alfano, G., Crisfield, M.A., 2001. Finite element interface models for the delamination analysis of laminated composites: mechanical and computational issues. Int. J. Numer. Methods Eng. 77 (2), 111–170.

Allix, O., Corigliano, A., 1996. Modelling and simulation of crack propagation in mixed-modes interlaminar fracture specimens. Int. J. Fract. 77, 111–140.

Allix, O., Ladeveze, P., Corigliano, A., 1995. Damage analysis of interlaminar fracture specimens. Compos. Struct. 31, 66–74.

Anon., 1996. Abaqus 6.2 User's Manual, Abaqus Inc., Pawtucket, USA.

Barenblatt, G., 1962. The mathematical theory of equilibrium cracks in brittle fracture. Adv. Appl. Mech. 7, 55–129.

Bažant, Z.P., Jirásek, M., 2002. Nonlocal integral formulations of plasticity and damage: survey of progress. J. Eng. Mech. 128, 1119–1149.

Belytschko, T., Liu, W.K., Moran, B., 2001. Nonlinear Finite Elements for Continua and Structures. John Wiley & Sons, Ltd.

Benzeggagh, M.L., Kenane, M., 1996. Measurement of mixed-mode delamination fracture toughness of unidirectional glass/epoxy composites with mixed-mode bending apparatus. Compos. Sci. Technol. 49, 439–449.

Borg, R., Nilsson, L., Simonsson, K., 2002. Modeling of delamination using a discretized cohesive zone and damage formulation. Compos. Sci. Technol. 62, 1299–1314.

Camanho, P.P., Matthews, F.L., 1999. Delamination onset prediction in mechanically fastened joints in composite laminates. J. Compos. Mater. 33, 906–927.

Camanho, P.P., Dávila, C.G., de Moura, M.F., 2003. Numerical simulation of mixed-mode progressive delamination in composite materials. J. Compos. Mater. 37 (16), 1415–1438.

Camanho, P.P., Dávila, C.G., Pinho, S.T., 2004. Fracture analysis of composite co-cured structural joints using decohesion elements. Fatigue Fract. Eng. Mater. Struct. 27, 745–757.

Chaboche, J.L., Girard, R., Schaff, A., 1997. Numerical analysis of composite systems by using interphase/interface models. Comput. Mech. 20, 3–11.

Chen, J., Crisfield, M.A., Kinloch, A.J., Busso, E.P., Matthews, F.L., Qiu, Y., 1999. Predicting progressive delamination of composite material specimens via interface elements. Mech. Compos. Mater. Struct. 6, 301–317.

Crews, J.H., Reeder, J.R., 1988. A mixed-mode bending apparatus for delamination testing. NASA TM 100662.

Cui, W., Wisnom, M.R., 1993. A combined stress-based and fracture-mechanics-based model for predicting delamination in composites. Composites 24, 467–474.

Dávila, C.G., Johnson, E.R., 1993. Analysis of delamination initiation in postbuckled dropped-ply laminates. AIAA J. 31, 721–727.

Dávila, C.G., Camanho, P.P., de Moura, M.F.S.F., 2001. Progressive Damage Analyses of Skin/Stringer Debonding. Proceedings of the American Society for Composites 16th Technical Conference, Blacksburg, VA, September 9–12.

Dugdale, D.S., 1960. Yielding of steel sheets containing slits. J. Mech. Phys. Sol. 8, 100–104.

Goyal-Singhal, V., Johnson, E.R., Dávila, C.G, Jaunky, N., 2002. An irreversible constitutive law for modeling the delamination process using interface elements. In: 43rd AIAA/ASME/ASCE/AHS/ASC Structures, Structural Dynamics and Materials Conference, Colorado, USA.

Goyal-Singhal, V., Johnson, E.R., Dávila, C.G., 2004. Irreversible constitutive law for modeling the delamination process using interfacial surface discontinuities. Compos. Struct. 64, 91–105.

Griffith, A.A., 1921. The phenomena of rupture and flow in solids. Philos. Trans. Roy. Soc., London, Ser. A 221, 163–198.

Hellen, T.K., 1975. On the method of the virtual crack extension. Int. J. Numer. Methods Eng. 9, 187–207.

Hillerborg, A., Modéer, M., Petersson, P.E., 1976. Analysis of crack formation and crack growth in concrete by means of fracture mechanics and finite elements. Cement Concr. Res. 6, 773–782.

Irwin, G.R., 1957. Analysis of stresses and strains near the end of a crack transversing a plate. J. Appl. Mech. 24, 361–366.

Jansson, N.E., Larsson, R., 2001. A damage model for simulation of mixed-mode delamination growth. Compos. Struct. 53, 409–417.

Krueger, R., 2002. The virtual crack closure technique: history, approach and applications. NASA/CR-2002-211628.

Krueger, R., Cvitkovich, M.K., O'Brien, T.K., Minguet, P.J., 2000. Testing and analysis of composite skin/stringer debonding under multi-axial loading. J. Compos. Mater. 34, 1263–1300.

Ladevèze, P., Allix, O., Gornet, L., Lévêque, D., et al., 1998. A computational damage mechanics approach for laminates: identification and comparisons with experimental results. In: Voyiadkjis, G.Z., Ju, J.W.W., Chaboche, J.L. (Eds.), Damage Mechanics in Engineering Materials. Elsevier Science B.V., pp. 481–499.

Larsson, R., Jansson, N., 2002. Geometrically non-linear damage interface based on regularized strong discontinuity. Int. J. Numer. Methods Eng. 54, 473–497.

Li, J., 2000. Three-dimensional effects in the prediction of flange delamination in composite skin-stringer pull-off specimens. In: 15th Conference of the American Society for Composites Texas, USA.

Li, J., Sen, J.K., 2000. Analysis of frame-to-skin joint pull-off tests and prediction of the delamination failure. In: 42nd AIAA/ASME/ASCE/AHS/ASC Structures, Structural Dynamics and Materials Conference, Seattle, WA, USA.

Li, D., Wisnom, M., 1994. Modelling damage initiation and propagation composites using interface elements. Presented at the Computer Aided Design in Composite Material Technology—International Conference, Southampton, UK.

Liu, S., 1999. Quasi-impact damage initiation and growth of thick-section and toughened composite material. Int. J. Solids Struct. 31, 3079–3098.

Mazars, J., 1982. Mechanical damage and fracture of concrete structuresAdvances in Fracture Research (Fracture 81), vol. 4. Pergamon Press, Oxford, pp. 1499–1506.

Mi, Y., Crisfield, M.A., 1996. Analytical derivation of load/displacement relationship for the DCB and MMB and proof of the FEA formulation. Internal Report, Department of Aeronautics, Imperial College London.

Mi, U., Crisfield, M.A., Davies, G.A.O., 1998. Progressive delamination using interface elements. J. Compos. Mater. 32, 1246–1272.

Needleman, A., 1987. A continuum model for void nucleation by inclusion debonding. J. Appl. Mech. 54, 525–532.

Oliver, J., Cervera, M., Oller, S., Lubliner, J., 1990. Isotropic damage models and smeared crack analysis of concrete. In: Second International Conference on Computer Aided Analysis and Design of Concrete Structures, vol. 2, pp. 945–958.

Ortiz, M., Pandolfi, A., 1999. Finite-deformation irreversible cohesive elements for three-dimensional crack propagation analysis. Int. J. Numer. Methods Eng. 44, 1267–1282.

Parks, D.M., 1974. A stiffness derivative finite element technique for determination of crack tip stress intensity factors. Int. J. Fract. 10 (4), 487–502.

Petrossian, Z., Wisnom, M.R., 1998. Prediction of delamination initiation and growth from discontinuous plies using interface elements. Composites Part A 29, 503–515.

Raju, I.S., 1987. Calculation of strain-energy release rates with higher order and singular finite elements. Eng. Fracture Mech. 38 (3), 251–274.

Reddy Jr., E.D., Mello, F.J., Guess, T.R., 1997. Modeling the initiation and growth of delaminations in composite structures. J. Compos. Mater. 31, 812–831.

Reeder, J.R., Crews, J.H., 1990. Mixed-mode bending method for delamination testing. AIAA J. 28, 1270–1276.

Reeder, J.R., Crews, J.H., 1991. Nonlinear analysis and redesign of the mixed-mode bending delamination test. NASA TM 102777.

Rice, J.R., 1968. A path independent integral and the approximate analysis of strain concentration by notches and cracks. J. Appl. Mech. 35, 379–386.

Rybicki, E.F., Kanninen, M.F., 1977. A finite element calculation of stress intensity factors by a modified crack closure integral. Eng. Fracture Mech. 9, 931–938.

Schellekens, J.C.J., de Borst, R., 1993. A nonlinear finite-element approach for the analysis of mode-I free edge delamination in composites. Int. J. Solids Struct. 30 (9), 1239–1253.

Schellekens, J.C.J., de Borst, R., 1992. On the numerical integration of interface elements. Int. J. Numer. Methods Eng. 36, 43–66.

Simo, J., Ju, J.W., 1987a. Strain- and stress-based continuum damage model—I. Formulation. Int. J. Solids Struct. 23, 821–840.

Simo, J., Ju, J.W., 1987b. Strain- and stress-based continuum damage model—II. Computational aspects. Int. J. Solids Struct. 23, 841–869.

Tvergaard, V., Hutchinson, J.W., 1992. The relation between crack growth resistance and fracture process parameters in elastic–plastic solids. J. Mech. Phys. Solids 40, 1377–1397.

Tvergaard, V., Hutchinson, J.W., 1993. The influence of plasticity on mixed-mode interface toughness. J. Mech. Phys. Solids 41, 119–1135.

Wu, E.M., Reuter Jr., R.C., 1965. Crack extension in fiberglass reinforced plastics. T&AM Report No. 275, University of Illinois.

Xu, X.-P., Needleman, A., 1994. Numerical simulations of fast crack growth in brittle solids. J. Mech. Phys. Solids 42 (9), 1397–1434.

Yan, A.M., Marechal, E., Ngyen-Dang, H., 2001. A finite-element model of mixed-mode delamination in laminated composites with and R-curve effect. Compos. Sci. Technol. 61, 1413–1427.

Ye, L., 1988. Role of matrix resin in delamination onset and growth in composite laminates. Compos. Sci. Technol. 33, 257–277.

Zou, Z., Reid, S.R., Li, S., Soden, P.D., 2001. Mode separation of energy release rate for delamination in composite laminates using sublaminates. Int. J. Solids Struct. 38, 2597–2613.

Zou, Z., Reid, S.R., Li, S., Soden, P.D., 2002. Modelling interlaminar and intralaminar damage in filament wound pipes under quasi-static indentation. J. Compos. Mater. 36, 477–499.